Dielectric properties of thin Cr_2O_3 films grown on elemental and oxide metallic substrates

Ather Mahmood*[1], Michael Street*[1], Will Echtenkamp[1], Chun Pui Kwan[2], John P. Bird[2,3], and Christian Binek[1]

[1] Department of Physics and Astronomy, Theodore Jorgensen Hall, University of Nebraska-Lincoln, Lincoln, NE 68588-0299, USA

[2] Department of Physics, University at Buffalo, the State University of New York, Buffalo, NY 14260-1500

[3] Department of Electrical Engineering, University at Buffalo, the State University of New York, Buffalo, NY, 14260-1900

* Equal contribution

Abstract

In an attempt to optimize leakage characteristics of α- Cr_2O_3 thin films, its dielectric properties were investigated at local and macroscopic scale. The films were grown on Pd (111), Pt (111) and V_2O_3 (0001), supported on Al_2O_3 substrate. The local conductivity was measured by conductive Atomic-Force-Microscopy (C-AFM) mapping of Cr_2O_3 surfaces which revealed the nature of defects that formed conducting paths with the bottom Pd or Pt layer. A strong correlation was found between these electrical defects and the grain boundaries revealed in the corresponding topographical scans. In comparison, the Cr_2O_3 film on V_2O_3 exhibited no leakage paths at similar tip bias value. Electrical resistance measurements through e-beam patterned top electrodes confirmed the resistivity mismatch between the films grown on different electrodes. The X- ray analyses attributes this difference to the twin free Cr_2O_3 growth on V_2O_3 seeding.

I. INTRODUCTION

The use of an applied electric field to manipulate magnetism in the absence of dissipative electric currents has recently drawn much attention. It promises a new class of low-power spintronic devices taking advantage of non-volatile magnetic order [1-2]. A promising scheme for such manipulation involves the electrical control of magnetization via the exchange bias (EB) [3] effect, which can be used to switch the remnant magnetization of a ferromagnetic thin film. EB arises from exchange coupling at the interface between an antiferromagnet and a ferromagnet, and causes the hysteresis loop of the ferromagnet to shift along the field axis. Chromia (Cr_2O_3) is a magnetoelectric (ME) antiferromagnet [4-5] that can be used to realize a particular variation of the ordinary EB effect known as voltage-controlled EB. Chromia

has a Néel temperature (T_N) of 307 K. Isothermal voltage-control of EB has been demonstrated at room temperature utilizing bulk single crystals of this insulating antiferromagnet [6-7]. B-doped chromia may even be a candidate for high T_N magnetoelectrics [8] while both intrinsic and B-doped forms of this material are of interest for use in low-power magnetic random access memory [4-5]. Practical device applications require a thin-film implementation of this material. Voltage control of EB has been achieved in magnetic heterostructures incorporating thin-film chromia [9-13]. However, reversible electrical switching of EB between positive and negative EB fields larger than the coercivity of the loop with applied magnetic fields lower in magnitude than the coercive fields, remains a significant challenge. Optimization of the magnetic and electrical properties of the magnetoelectric films is required in order to overcome this challenge.

The central concept that lies at the heart of utilizing chromia for the electrical control of magnetism involves reversing the polarity of the EB generated at its interface with a ferromagnet. In the isothermal version of this switching, static electric (E_{iso}) and magnetic (H_{iso}) fields are applied simultaneously across the chromia along its *c*-axis. Once EB has first been initialized via a ME field cooling procedure, i.e., cooling from above the Néel temperature (T_N = 307 K) to below it, with the simultaneous applications of static electric and magnetic fields. The field product ($E_{iso}H_{iso}$) determines the condition under which switching occurs [7, 14]. It is therefore possible to achieve switching for weak magnetic fields by increasing E_{iso} accordingly. This should effectively allow for the practical control of magnetism via purely electrical means. The small required symmetry breaking magnetic field can be utilized for instance from the fringe magnetic fields emanating from the fixed ferromagnetic film in a magnetic tunnel junction (MTJ) used for read-out. The MTJ uses tunnel magneto-resistance to read the bit in a Magnetoelectric Random Access Memory (MERAM) architecture. The difficulty with this approach, however, is that it requires the chromia films to be able to support large electric fields (> 10 kV/mm), without exhibiting significant leakage. It would not only obviate any potential power gains expected to arise from the voltage-based control of magnetism but also induce dielectric breakdown of the ME film. It is worth to mention that all thin film heterostructures require much higher field products for switching than their bulk counterpart. The reason for this is the fact that, in thin films, one must overcome additional exchange coupling in one direction (while the switching is supported by exchange in the other direction). This makes the switching product more asymmetric, while the reduced volume of the antiferromagnet additionally means that less ME energy is available to switch the ferromagnet. Under such conditions, the switching-field product is no longer an intrinsic property of chromia, but is rather strongly affected by its coupling to the ferromagnet [13].

The preceding discussion implies that a critical parameter for evaluating the performance of chromia films is their electrical resistivity. For the EB-based applications that we have described, it is essential that current leakage through the biased films should be reduced to an absolute minimum. In bulk, at least, chromia has a measured band-gap of 3.3 eV [15] that provides it with high intrinsic resistivity, $\rho \sim 10^{12}$ Ω-cm at 300 K [16]. Thin films produced previously, via a variety of different techniques, approach nowhere near this optimal value with reported resistivities ranging from $10^2 - 10^9$ Ω-cm [11, 12, 17]. Generally, in the case of transition-metal oxides, it is known that regardless of the specific growth method used, proper choice of metal substrate can have a profound effect on the surface structure of the resulting oxide film and its electrical properties [18]. Motivated by this understanding, in this article we explore the structural and electrical properties of chromia films prepared on Pd (111), Pt (111) and V_2O_3 (0001) seed layers. In most studies cited in this work, Pt and Pd have remained the choice materials to be used as both seed layers and bottom electrode. In contrast, V_2O_3 grown by sputtering is recently pioneered in this study [19] as the seed layer and the bottom gate material for Chromia. The rationale for studying chromia on three distinct seed layers is to elucidate the role of different degrees of crystalline twinning and lattice deformation on the electric conduction pattern in a top-to-bottom device configuration. Our investigation reveals that the benefits of using V_2O_3 as the seed layer is two-fold. First, V_2O_3, as opposed to the cubic materials Pd and Pt, is isostructural with the corundum Al_2O_3 (spacegroup R-3c) substrate. This pseudo-homoepitaxy promotes growth of films that are free of rotational defects, but are unavoidable in the growth of Pd and Pt on Al_2O_3 [20]. These rotational domains will be discussed in further detail later. Second, V_2O_3 is used because of the small lattice mismatch (~0.1%), as compared with Pd(3.9%) and Pt(3.1%), with chromia that minimizes the strain on the chromia films. The V_2O_3 films are grown at a thickness above the critical thickness for relaxation [21] to avoid significant strain in the chromia films. These relationships emphasize the benefits in using V_2O_3 as bottom electrode to optimize the properties of chromia thin films for device applications. It is also important to note that V_2O_3 thin films exhibit a Metal-Insulator Transition (MIT) at about 150K [21]. Below this temperature, an antiferromagnetic insulating state is observed. It is characterized by several orders of magnitude increase in resistivity. At temperatures above 200 K, V_2O_3 behaves like a bad metal with virtually constant resistivity of about 10^{-3} Ω-cm. The MIT is shifted towards lower temperature with decreasing film thickness. This is beneficial for device applications which utilize metallicity of V_2O_3 as bottom contact and substrate for defect free growth of chromia.

In addition to performing a variety of structural characterizations on these films, we also investigate their electrical properties via electrical resistivity measurements and conductive Atomic-Force-Microscopy (C-

AFM). Lithographic patterning is used to form electrical contacts on chromia with sizes ranging from 1 μm^2 to close to 1 mm^2, and is found to reveal dramatic differences in current leakage based on metallic seed layer. More specifically, Pd-based films exhibit wide and uncontrolled variations in leakage at levels that vary by many orders of magnitude and show pinhole-based inhomogeneity, whereas Pt-based films, though more homogenous in resistivity, demonstrate low values as well. The afore-mentioned problems are absent in the V_2O_3-based films. Microscopic insight into the reasons for these very different behaviors is provided by using conductive atomic force microscopy (C-AFM) to correlate leakage in the films to the presence of microscopic defects in their surfaces. In this way we identify the presence of a class of defects which mediate leakage in the Pd-based films. C-AFM also presents an improved topography and reduced leakage in the case of Pt-based films, but demonstrates the presence of an extremely smooth surface of V_2O_3-based films with insulating surface shown in the corresponding conductivity mapping. This result is supported by our X-ray diffraction (XRD) studies. These studies reveal dominant presence of 60° rotational domains in Pd-based films, significant reduction of these domains for Pt-based films and total absence of these domains in V_2O_3-based films. By demonstrating the critical influence that the metal seed layer may exert on the dielectric properties of the resulting chromia layers, our results represent a crucial step towards the realization of electrically contacted chromia films with virtually bulk-like resistivity critical for the realization of voltage-controlled spintronic applications.

II. EXPERIMENT

The samples studied consist of 5, 20, 40 and 300 nm chromia films grown onto (0001) sapphire substrates. Prior to chromia film growth, a bottom metallic electrode (Pd, Pt, or V_2O_3) was deposited. The sapphire substrates were cleaned using a modified Radio Corporation of America protocol [22] and introduced into an ultra-high vacuum chamber. For Pd electrode, 1nm of it was first deposited on sapphire (0001) via Molecular Beam Epitaxy at 300 °C substrate temperature and deposition rate was 0.5 nm/min. Additional Pd was then grown in a three-step growth process [23] as follow: 1. A seed layer of 7 nm was grown at 650 °C. 2. The sample was then cooled to 50 °C, and an additional 33 nm of Pd was deposited at a rate of 0.008 nm/s. 3. To crystalize the Pd, the temperature was raised to 650 °C. This process minimized the roughness of the final film.

Pt electrodes were deposited using DC magnetron sputtering. The films were fabricated at room temperature using a power of 20W in an Ar atmosphere of 3mTorr from a base pressure of about $1x10^{-7}$

Torr and the deposition rate was about 0.4 nm/min. The Pt films were then annealed at 600 °C to smoothen the surface and ensure good crystallinity.

The V_2O_3 electrodes were deposited using pulsed laser deposition (PLD). The substrates were heated to 750 °C during the deposition. A KrF excimer laser with pulse energies of 170 mJ, a spot size of about 6 mm^2 and a pulse width of 20 ns (at a repetition rate of 6 Hz) was used to ablate a V_2O_3 target. The target-to-substrate distance was kept at about 9 cm and the substrates rotation rate was at 3 rpm.

Cr_2O_3 was then grown on to the resulting substrates (described above) *ex-situ* using PLD. The pulse energy was 200 mJ and the frequency was 10 Hz from a Cr_2O_3 target. The temperature of the substrate was maintained at 500 °C during deposition of the chromia films. The growth rate of Cr_2O_3 (V_2O_3) was about 0.025 nm/s (0.017 nm/s). For samples with Pd electrodes, chromia was grown on four substrates with thickness of 5-, 20-, 40- and 300-nm of Pd. These samples were compared with a 300-nm thick chromia film grown on a 25nm thick Pt and a 20-nm chromia film grown on 20nm thick V_2O_3.

X-ray diffraction (XRD) was used to study the structural properties of the films. Cu $K_{\alpha 1}$ x-ray radiation with a wavelength of 1.54 Å was used to perform x-ray analysis in various modes. Those are θ-2θ Bragg reflection for out-of-plane scans, phi (ϕ) scans for determining rotational domains, and in-plane $2\theta_{\chi/\phi}$ diffraction. Electrical leakage measurements were performed on lithographically formed contacts using Keithley 2400 sourcemeter.

Conductive AFM studies were performed under ambient conditions using a Bruker Icon AFM in tunneling AFM (TUNA) mode, with a current sensing C-AFM module. PtIr coated Si-tips with a nominal radius of 20-40 nm and a spring constant of 2.8 N/m were used. The current sensitivity was set at 20 pA/V. To ensure a dry environment, all topography and electrical measurements were recorded under a constant flow of N_2. Since the structure of the tip, including its shape and radius, can be worn out both mechanically and electrically as successive scans are performed, care was taken to acquire images with fresh tips whenever such degradation was noticeable. Usually, during current mapping by scanning probe, the observed variations depend greatly on cantilever deflection and the tip condition. A constant cantilever deflection set point of 30 nN was utilized during all imaging. The DC voltage was applied between the bottom electrode and tip, with the latter acting as a virtual ground.

III. RESULTS AND DISCUSSION

In Fig. 1, we show the results of the out-of-plane XRD θ-2θ scans for (a) chromia(300)/Pd(40)/Al_2O_3, (b) chromia(300)/Pt(20)/Al_2O_3 and (c) chromia(20)/V_2O_3(20)/Al_2O_3 heterostructures (where the numbers in parentheses represent film thickness in nanometers). Full scans were performed to confirm the (0001)-orientation of the chromia and V_2O_3 films, and the (111)-texture for Pd and Pt films. For clarity, we only show the first order Bragg diffraction peaks. Due to the inability to distinguish the first order diffraction peaks of chromia and Pt, in-plane $2\theta_{\chi/\phi}$ diffraction was performed on this sample to confirm the epitaxy of the chromia layer. It is important to note that the Laue oscillations in the data of Fig. 1(b) are from the Pt film and not from the chromia film. We attempted to fit the data and the fit provides a thickness close to the expected 20nm value. Also, the data shown in Fig. 1(c) exhibit Laue oscillations for both the Cr_2O_3(20) and V_2O_3(20) films.

ϕ -scans were performed to investigate the presence of 60° rotational domains in the films, as shown in Fig. 2. In these measurements, the samples were tilted such that the scattering vector is normal to the $(10\bar{1}4)$ planes for the chromia and V_2O_3 films. For the Pd and Pt films, the samples were tilted so that the scattering vector is normal to the $(11\bar{1})$ planes. Following this alignment, the samples were rotated about the sample normal with the source and detector fixed at the appropriate Bragg angles for each film. This type of scan manifests the presence of in-plane rotational domains in thin films. Fig. 2 shows the φ-scans for chromia growth on (a) Pd, (b) Pt and (c) V_2O_3. Both the Pd and Pt films exhibit essentially no preference in growth. This is indicated by the six-fold symmetry of the φ-scans with each peak nearly equally intense separated by 60°. A (111)-oriented Pd or Pt single crystal would have three-fold symmetry in this type of scan. These rotational domains are formed at the Pd (or Pt)/Al_2O_3 interface and propagate vertically through the heterostructure. The growth of cubic structured Pd/Pt on a hexagonal plane of Al_2O_3 with epitaxial relationship [111]||[0001] has no preference in the two rotational domain formations [20]. In contrast, the V_2O_3 film has no indications of rotational domains. Additionally, the ϕ -scans of chromia for each sample show fairly similar behavior as the seed layer. For example, in Fig. 2(a), each rotational domain is labeled 'A' and 'B'. Corresponding domain peaks are separated by 120°. For the sample with a Pd seed layer, the chromia shows nearly equal presence of these domains, whereas the sample with Pt, shows significant reduction of these domains. Finally, the chromia film grown on V_2O_3 eliminates these domains completely. It should be noted that, in this type of scan, it is impossible to distinguish whether these domains are twins or other types of domains involving 60° rotation.

Next, we will present and discuss the electrical conduction and topography of these films via scanning probe studies. Fig. 3 compares the results of lateral topographic, and corresponding current mapping of two Pd-based chromia films, of thickness 5nm (Fig. 3(a)) and 20nm (Fig. 3(b)). The topographical image of the 5-nm film (Fig. 3(a)) reveals the clear presence of flat planes that are unconnected to one another. These unconnected flat planes are referred to as r-planes and their formation is a consequence of the low surface energy of chromia [24]. An analysis of a 100 × 100 nm^2 area on a single plane reveals a root mean square (rms) surface roughness of ~0.24 nm. Also, there are space between flat planes and they maintain a depth of around 5 nm, indicating that the bottom Pd electrode is being exposed in these areas. This is further confirmed in the corresponding C-AFM mapping in Fig. 3(b), which yields a current level of several pA on these low lying areas, whereas the chromia planes are completely insulating at a tip bias of 1V. Fig. 3(c) shows a topographic image of a 20-nm chromia film formed on Pd. One can observe here that the flat planes join together to form a more continuous surface, although some pinholes are left in-between them. One noticeable feature that now starts to appear is the presence of high structures (typically few tens of nm high), referred to here as mesas, which display similar edge orientations to the chromia planes. In Fig. 3(d), which shows the corresponding current map of Fig. 3(c), the mesas are mostly leaky at their edges, although it is not clear whether this leakage is intrinsic. There are other type of surface defects, which are present in abundance, that are responsible for excessive leakage. These defects appear as small dots in the topographic image of Fig. 3(c), and are correlated directly to the highly conductive spots in the C-AFM image of Fig. 3(d). Such conduction spots are not uncommon in transition metal oxides, in which they are generally considered to represent the location of conducting filaments in the oxide [25] [26] [27] [28]. There have been numerous studies of current sensing in contact mode using scanning probe microscopy, on resistive switching memories based on transition metal oxides, where the migration of O_2- ions and the remaining oxygen vacancies are responsible for the formation of conducting nanofilaments [29]. C-AFM can detect the presence of these filaments and can even be used to bias them in low or high resistive states. Figs. 4(a) and 4(b) show topography and conductive maps, respectively, for a 40-nm thick Pd-based chromia film. As can be clearly seen, the flat planes are now joined together but the conducting filaments and mesas still exist. The corresponding C-AFM map now shows leakage that is predominantly mediated through the spots.

Turning now to thicker films, in Figs. 4(c) and 4(d) we show topography and C-AFM maps, respectively, obtained for a 300-nm thick Pd-based chromia film. It is notable that the topographical features obtained in this case resemble those exhibited by the 40-nm film, with flat planes that are completely joined together. Both the height and the abundance of the aforementioned mesas are also reduced as compared

to thinner films. The corresponding conductive mapping shows some remarkable features. The boundaries between the flat planes clearly exhibit enhanced leakage and can be readily correlated with the topographical grain boundaries. Upon close inspection, one observes that these are individual conducting dots lined along the grain boundaries. The dotted line indicated in the topographical image follows the shape of one such boundary. Leakage at grain boundaries is not uncommon and has been observed in C-AFM studies of other oxides [30]. The leakage has been explained by considering that the nanoscale conducting paths formed at the grain boundaries can serve as channels for easy diffusion for oxygen vacancies. In other cases of resistive switching, consideration has been given to models based on charge carrier trapping [31], and of a Mott transition that is induced by carrier doping at the oxide-metal interface [31]. A structural study performed by our collaborators on 300-nm Pd-based chromia films helps explain the leakage through the grain boundaries [32]. They have combined advanced scanning transmission electron microscopy (STEM) characterization and density functional theory (DFT) to correlate structure and structural defects with their respective electronic properties. By using high-angle annular dark field STEM imagery, vertical planar grain boundaries with substantially reduced electronic band gap have been revealed [32]. They are prone to dielectric breakdown once electrons in the presence of an applied electric field gain sufficient energy to cross the reduced bandgap. This explains the observed high conduction points along the boundaries of flat planes in our 300-nm films. Although the lateral resolution of the AFM tip is less than that in STEM, and so is consequently unable to capture the <50-nm grains, the C-AFM mapping does show certain features that are not discernible in the corresponding topography map. The blue arrows in Fig. 4(d), for example, point to some of the smallest grains, for which C-AFM shows measurable structure even though the corresponding topographical features are not well resolved.

To shed further light on the conduction behavior of the 300-nm films, both photolithography and electron-beam lithography were used to fabricate Cr/Au electrodes on top of Pd-based chromia. The contacts size vary from 500 × 500 μm^2 to 1 × 1 μm^2, thereby allowing us to control the number of leakage filaments in contact with the electrode. C-AFM was then used to characterize the current profile of these pads. Figs. 5(a) & 5(b) are the topographical and C-AFM images, respectively, obtained by scanning over a 5 × 5 μm^2 electrode, and a portion of a 10 × 10 μm^2 pad. At a scanning-tip voltage of 1.0 V, different current strengths of ~3 pA and 0.5 pA are clearly seen for these two electrodes. This difference in current strength indicates that the number of conducting paths in contact with any given electrode varies in accordance with its size. To further illustrate this point, in Table 1 we indicate the value of the current determined for contact pads of varying size, clearly revealing a direct relationship between this current and the contact area. This current is the total current determined over the total time that the tip remains in contact with the surface.

To draw a comparison between two representative electrode areas, we calculated resistivity of 5 x 5 μm² and 10 x 10 μm² electrodes and the corresponding values are 4.9×10^9 Ω-cm and 3.3×10^9 Ω-cm, which indicate a trend towards scaling, as will be more clear by the discussion in the next paragraph. This scaling of resistivity is traced to electrodes of very small sizes such as 1 μm² as shown in Fig 5 (c) (topography) and Fig 5 (d) (conductivity mapping) for 1 μm² sized electrode; where an average current of few 10s of fA at 1.0 V bias is discernable from the noise range of the instrument and depicts a very high resistivity, a strong indication of a lesser number of filaments in contact with this electrode.

In Fig. 6, we show the results of a detailed comparison of the leakage resistance of more than a hundred different electrodes of varying size formed on 300-nm chromia films on Pd, Pt and V_2O_3 substrates. The ordinate of this figure provides the measured resistivity versus electrodes areas. For all three film types, and for the largest pad size (500 × 500 μm²) studied, it is clear that there is significant leakage, placing an upper limit on the area over which chromia films can be synthesized with satisfactory dielectric properties. For smaller pad sizes, however, the difference between films on all three seeding layers becomes clearer. Pd based films are more leaky and subject to large statistical variations in resistivity. Pd-based chromia with a contact size of 50 × 50 μm², resistance values range from just 1 kΩ to as much as 1 GΩ, with the latter value implying a leakage level of 1 nA at 1 V bias. The tendency for the Pd-based films to show increasing resistivity value with decreasing contact size and this appears to be consistent with the results of our corresponding current-mapping studies, which hint at the reduced number of shunting paths in direct contact with the electrodes. On the other hand, Pt-based films exhibit a large and uniform resistivity; this makes them a candidate for more reliable contacts as the resistivity values are more stable, albeit remaining low at around 10^9 Ω-cm. V_2O_3 based films again exhibit a wider spread in resistivity for smaller contacts. However, the striking feature is that the measured resistivity is larger than 10^{12} Ω-cm, which is comparable to that of chromia bulk at room temperature.

While we have largely focused thus far on the topography and 2-D conductivity mapping of Pd-based films, we repeated similar measurements on 20-nm Pt and V_2O_3 seed layers. Fig. 7(a) display the topography of 300-nm chromia films on Pt seeding layer. The topography shows that the aforementioned r-planes are absent in these films, while the grains are much smaller (~ 50-100 nm) than those exhibited by the Pd-based films. Consistent with this, the rms roughness of the films is ~ 0.15 nm. The corresponding current scan in Fig 7(b) indicate almost no leakage at the surface, with only a few leakage spots being present, in which the current remains at sub-pA levels. These spots appear relatively high in the topographical scans and likely represent surface contaminants, rather than any capping of the conducting

filaments. The absence of significant leakage in the results of Fig. 7 (b) appears consistent with the behavior shown in Fig. 6, in which the Pt-based films show a far more uniform resistivity. Fig 7 (c) shows a topographic scan of 20 nm thick chromia on V_2O_3 and it can be readily observed that an ultra-smooth surface has been grown as compared to the metal-based samples. The rms roughness is estimated to be < 0.1 nm characterized by absence of surface features observed in the above-mentioned films. The corresponding conductive mapping that was taken at a tip bias of 3.0 volts, is essentially feature-less as well, to mention the completely insulating nature of the surface. This is a direct result of absence of in-plane rotational domains as explained earlier. Thus, from our topographical and electrical studies, we infer that the Pt- and V_2O_3-based chromia films show significantly lower density of leakage sites than their Pd-based counterparts. More specifically, based on our XRD studies, this dramatic improvement is attributed to the absence of leakage pinholes associated with twinning and 60° rotated planes, which were found to be abundant in chromia on Pd.

IV. CONCLUSIONS

In this work, we have compared the morphology and accompanying electrical properties of thin film chromia formed on Al_2O_3 substrates with different seed layers (Pd, Pt and V_2O_3) and at various thicknesses. Through XRD studies, we found that the appearance of rotational domains is strongly dependent upon the choice of underlying seed layer. C-AFM measurements further reveal the source of current leakage to be the existence of nanoscale conducting paths at grain boundaries. Although this work does not establish any correlation between the rotational domains and the nanoscale conducting paths, we found that rotational domains, as well as the resulting electrical leakage, are strongly suppressed when chromia is grown on Pt and V_2O_3, which is in agreement with our electrical study shown in Fig. 6. Furthermore, very thin (20 nm) chromia films grown on V_2O_3 present a completely revolutionized result where the films are able to sustain high electric fields with reduced top-to-bottom applied voltage. Our results suggest that all-oxide approach has great promises for implementation in ultra-low power ME MRAM and spintronic logic devices.

ACKNOWLEDGMENTS

This research was supported by the National Science Foundation, through grants NSF-ECCS 1740136 and MRSEC DMR-1420645, by the nCORE, a wholly owned subsidiary of the Semiconductor Research Corporation (SRC) and by MURI W911NF-16-1-0472 supported by the Army Research Office. The research is performed in part in the Nebraska Nanoscale Facility, Nebraska Center for Materials and Nanoscience, which is supported by the National Science Foundation under Grant No. NNCI: 1542182, and the Nebraska Research Initiative.

References

[1] P. A. Dowben, C. Binek, and D. E. Nikonov, in *Nanoscale Silicon Devices* edited by S. Oda and D. K. Ferry (CRC Press, Boca Raton, FL, 2015).
[2] C. Binek and B. Doudin, J. Phys. Condens. Matter **17**, L39 (2005).
[3] J. Nogués and I. K. Schuller, J. Magn. Magn. Mater. **192**, 203 (1999).
[4] W. Kleeman and C. Binek, *Magnetic Nanostructures*, Edited by H. Zabel and M. Farle (Springer Berlin, 2013).
[5] P. A. Dowben, C. Binek, and D. E. Nikonov, *Nanoscale Silicon Devices*, Edited by S. Oda and D.K. Ferry (CRC Press, Boca Raton, FL, 2015).
[6] P. Borisov, A. Hochstrat, X. Chen, W. Kleemann, and C. Binek, Phys. Rev. Lett. 94, 117203 (2005).
[7] X. He, Y. Wang, N. Wu, A. N. Caruso, E. Vescovo, K. D. Belashchenko, P. A. Dowben, and C. Binek, Nat. Mater. **9**, 579 (2010).
[8] M. Street et al, Appl. Phys. Lett. **104**, 222402 (2014)
[9] W. Echtenkamp and C. Binek, Phys. Rev. Lett. 111, 187204 (2013).
[10] S. M. Wu, S. A. Cybart, D. Yi, J. M. Parker, R. Ramesh, and R. C. Dynes, Phys. Rev. Lett. **110**, 067202 (2013).
[11] J. T. Heron, J. L. Bosse, Q. He, Y. Gao, M. Trassin, L. Ye, J. D. Clarkson, C. Wang, J. Liu, S. Salahuddin, D. C. Ralph, D. G. Schlom, J. Íñiguez, B. D. Huey, and R. Ramesh, Nature **516**, 370 (2014).
[12] T. Ashida, M. Oida, N. Shimomura, T. Nozaki, T. Shibata, and M. Sahashi, Appl. Phys. Lett. **106**, 132407 (2015).
[13] K. Toyoki, Y. Shiratsuchi, A. Kobane, C. Mitsumata, Y. Kotani, T. Nakamura, and R. Nakatani, Appl. Phys. Lett. **106**, 162404 (2015).
[14] T. Martin and J. Anderson, IEEE Trans. Magn. **2**, 446 (1966).
[15] P. J. Brown, J. B. Forsyth, E. Lelièvre-Berna, and F. Tasset, J. Phys. Condens. Matter **14**, 1957 (2002).
[16] C.-P. Kwan, R. Chen, U. Singisetti, and J. P. Bird, Appl. Phys. Lett. **106**, 112901 (2015).
[17] S.-H. Lim, M. Murakami, S. E. Lofland, A. J. Zambano, L. G. Salamancariba, and I. Takeuchi, J. Magn. Magn. Mater. **321**, 1955 (2009).
[18] K.-J. Lee, L.-W. Wang, T.-K. Chiang, and Y.-H. Wang, Materials **8**, 7191 (2015).
[19] T. Kosub, M. Kopte, R. Hühne, P. Appel, B. Shields, P. Maletinsky, R. Hübner, M. O. Liedke, J. Fassbender, O. G. Schmidt, and D. Makarov, Nat. Commun. **8**, ncomms13985 (2017).
[20] M. Grundmann, Phys. Status Solidi B **248**, 805 (2011).

[21] L. Dillemans, T. Smets, R. R. Lieten, M. Menghini, C.-Y. Su, and J.-P. Locquet, Appl. Phys. Lett. **104**, 071902 (2014).

[22] D. Zhang, Y. Wang, and Y. Gan, Appl. Surf. Sci. **274**, 405 (2013).
[23] T. Wagner, G. Richter, and M. Rühle, J. Appl. Phys. **89**, 2606 (2001).
[24] Appl. Phys. Express **7**, 093006 (2014).
[25] R. Waser and M. Aono, Nat. Mater. **6**, 833 (2007).
[26] K. Szot, W. Speier, G. Bihlmayer, and R. Waser, Nat. Mater. **5**, 312 (2006).
[27] M. Hwan Lee and C. Seong Hwang, Nanoscale **3**, 490 (2011).
[28] Yong-Mu Kim and Jang-Sik Lee. J. Appl. Phys. **104**, 114115 (2008)
[29] M.-J. Lee, S. Han, S. H. Jeon, B. H. Park, B. S. Kang, S.-E. Ahn, K. H. Kim, C. B. Lee, C. J. Kim, I.-K. Yoo, D. H. Seo, X.-S. Li, J.-B. Park, J.-H. Lee, and Y. Park, Nano Lett. **9**, 1476 (2009).
[30] Y.-M. Kim and J.-S. Lee, J. Appl. Phys. **104**, 114115 (2008).
[31] A. Sawa, Mater. Today **11**, 28 (2008).
[32] C. Sun, Z. Song, A. Rath, M. Street, W. Echtenkamp, J. Feng, C. Binek, D. Morgan, and P. Voyles, Adv. Mater. Interfaces, (2017), 1700172

Figures and figure captions

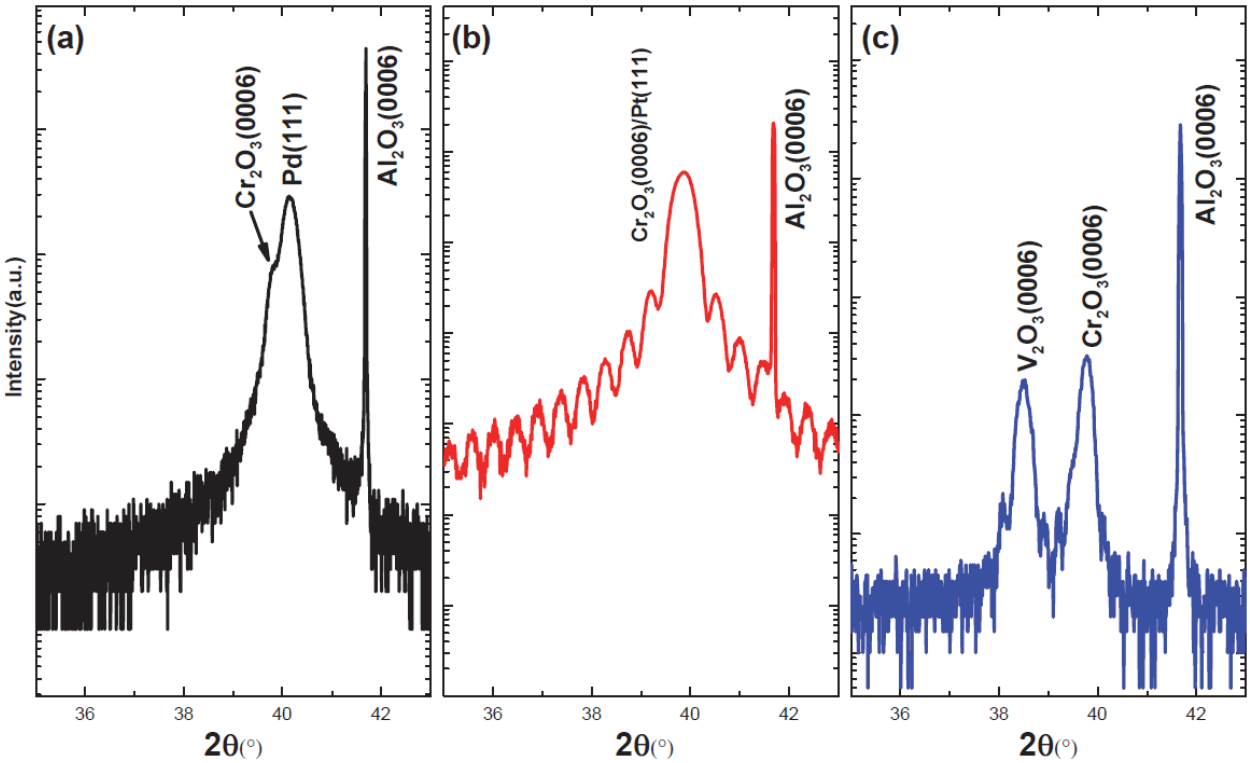

FIG. 1: Out-of-plane x-ray diffraction measurements of (a) Cr_2O_3(300nm)/Pd(40nm)/Al_2O_3, (b) Cr_2O_3(300nm)/Pt(20nm)/Al_2O_3 and (c) Cr_2O_3(20nm)/V_2O_3(20)/Al_2O_3. The Laue oscillations in (b) are from the Pt layer and not from the chromia film. It is also important to note that Laue oscillations are present in (c) for both the Cr_2O_3 and V_2O_3 films.

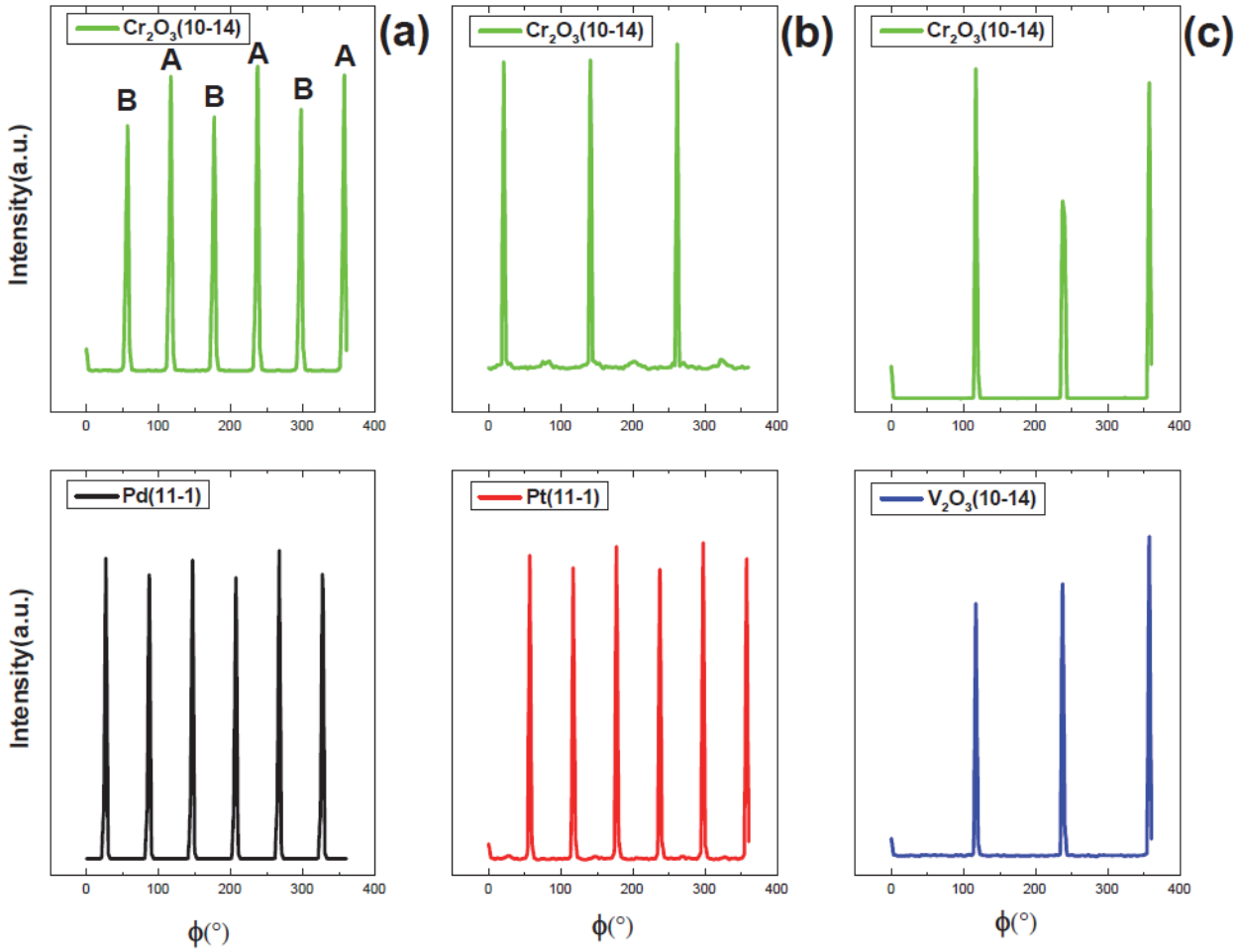

FIG. 2: Phi scans of the $(10\bar{1}4)$ pole of (a) chromia grown on Pd, (b) chromia grown on Pt and (c) chromia on V_2O_3. In panel (a), the in-plane rotational domains are labeled with 'A' and 'B' for the chromia phi scan. Each diffraction peak is separated by 60° for films with two domains and 120° for films with a single domain. For Pt and Pd films, the phi scans are done from the $(11\bar{1})$ planes.

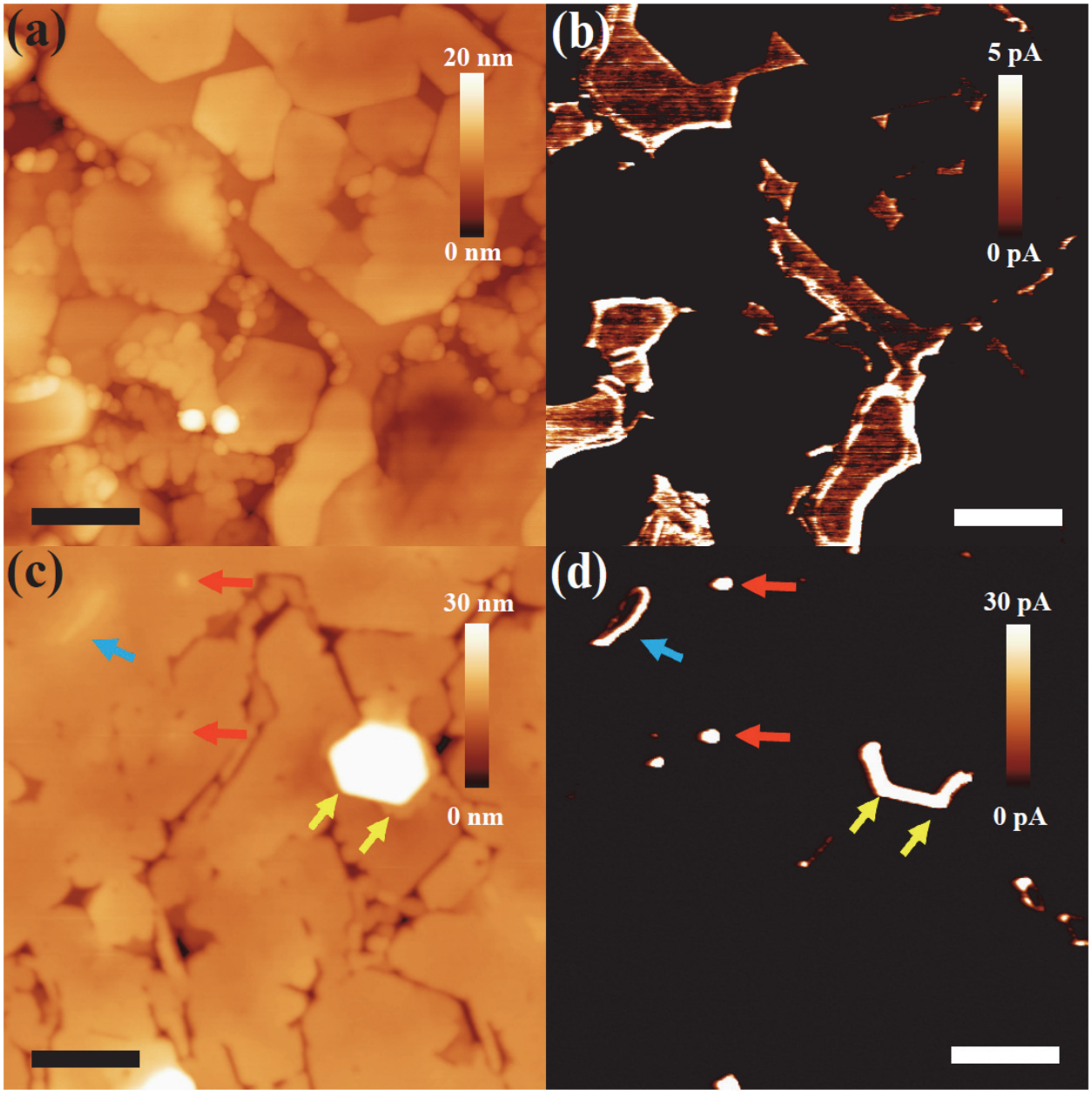

FIG. 3: Topography (a), (c) and conduction mapping (b), (d) of 5nm (a, b) and 20 nm(c, d) Cr_2O_3 (0001) film on Pd on Al_2O_3 substrate. The *r*-planes mentioned in the main text are seen in the topographic image in (a) as the flat planes with defined angles. The colored arrows in (b) and (d) point to various types of defects. Tip bias voltage for C-AFM is 1.0 V. Arrows in (c) and (d) point to various defects on the surface Scale bar: 200 nm.

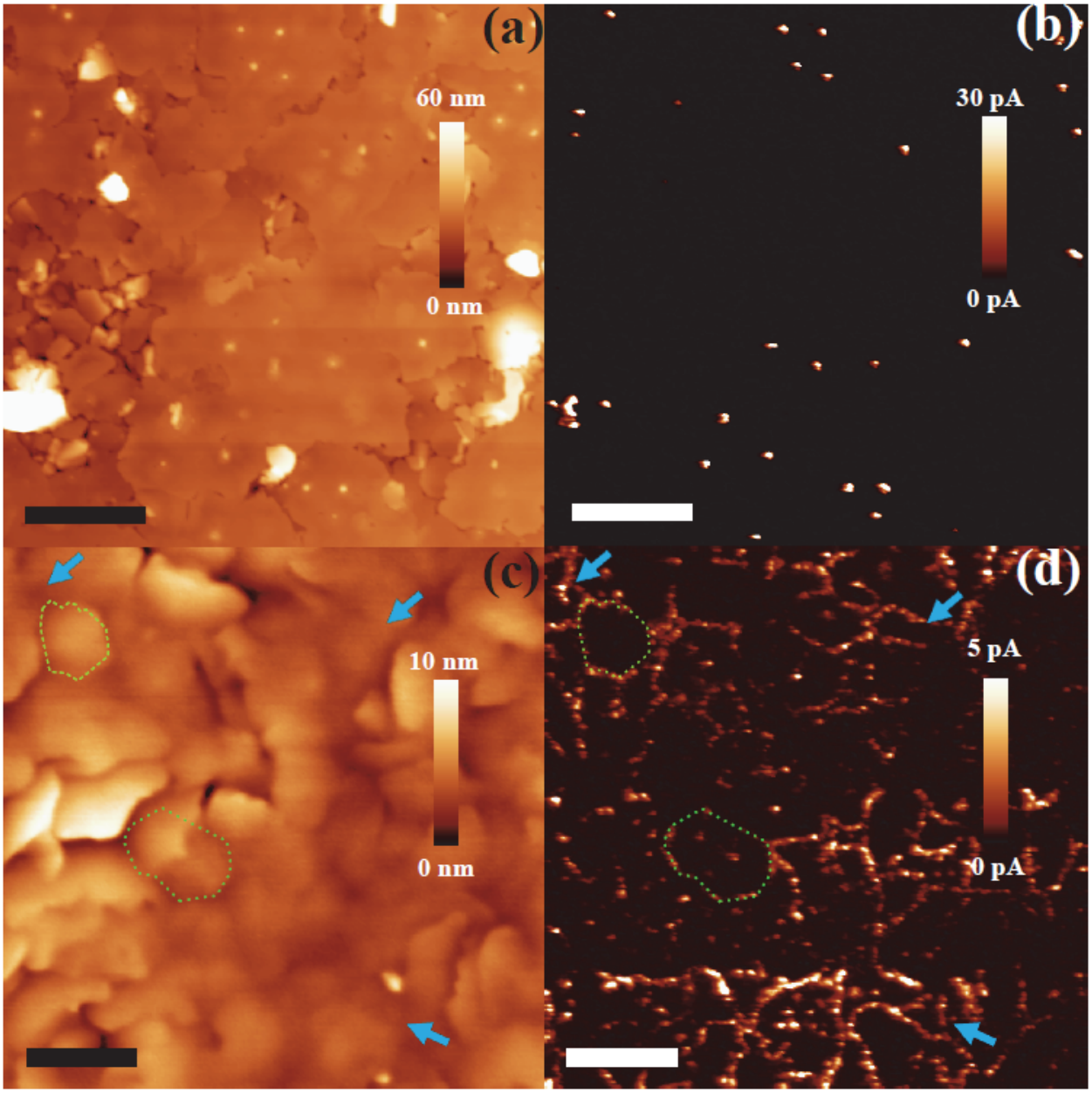

FIG. 4: Topography (a), (c) and conduction mapping (b), (d) of 40 nm (a) and 300 nm(c) Cr_2O_3 (0001) film on Pd on Al_2O_3 substrate. Tip bias voltage for C-AFM is 1.0 V. Arrows in (c) and (d) point to smaller-sized domains, whereas the area marked by the dotted line represents an individual grain. Scale bar: (a), (b): 800 nm. (c), (d): 200 nm.

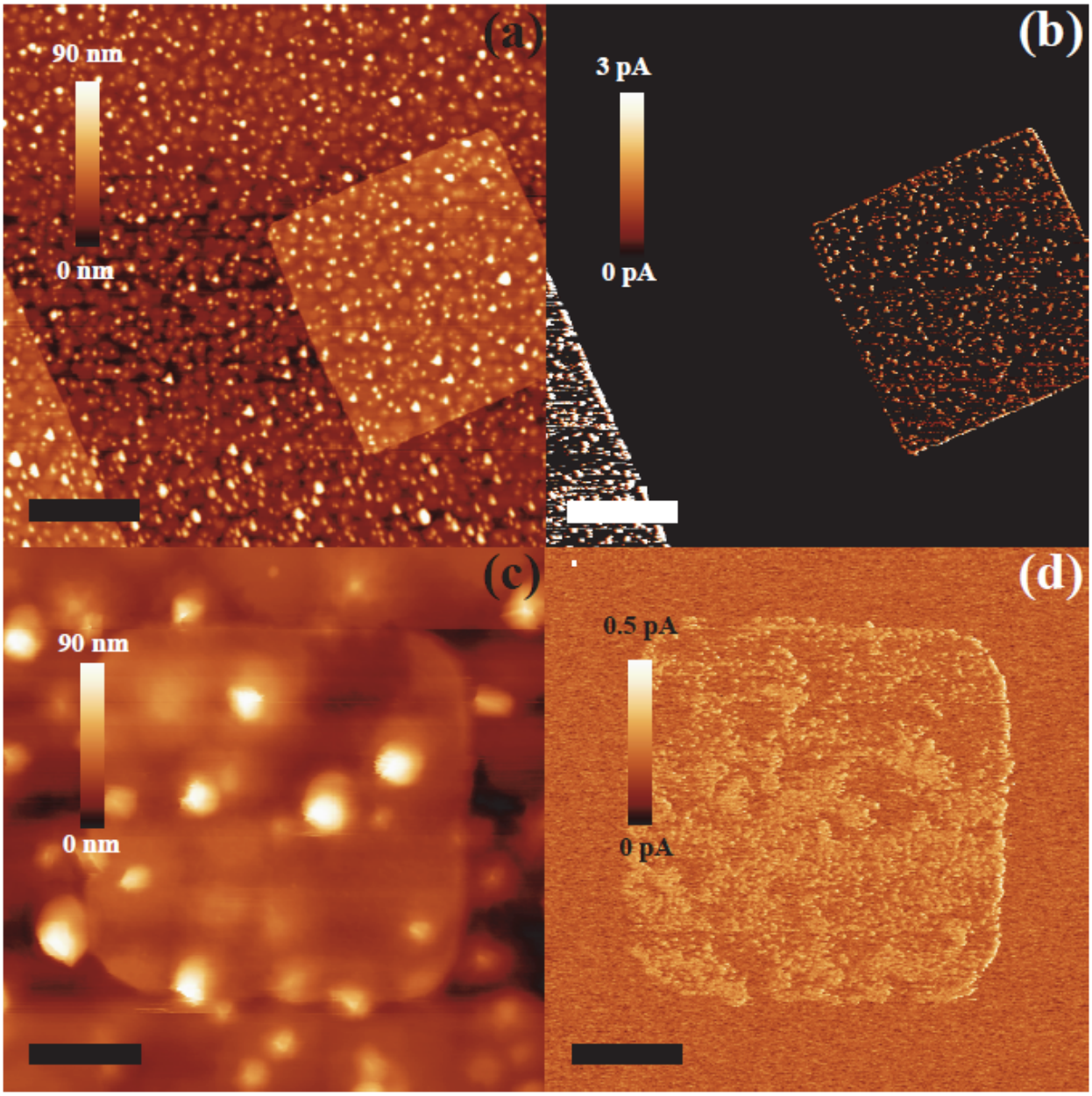

FIG. 5: (a) Topography and conduction mapping (b), (d) of electrodes of sizes 5 x 5 µm² and one portion of 10 x 10 µm² Ti/Au top electrodes on Cr_2O_3 (0001) film on Pd on Al_2O_3 substrate. (c) AFM topographic image of 1 x 1 µm² Ti/Au pad on Cr_2O_3 (0001) film on Pd on Al_2O_3 substrate. The C-AFM image in this case (d) represents almost negligible current of ~0.1 pA. Tip bias voltage for C-AFM is 1.0 V. Scale bar: (a), (b): 2 µm. (c), (d): 300 nm.

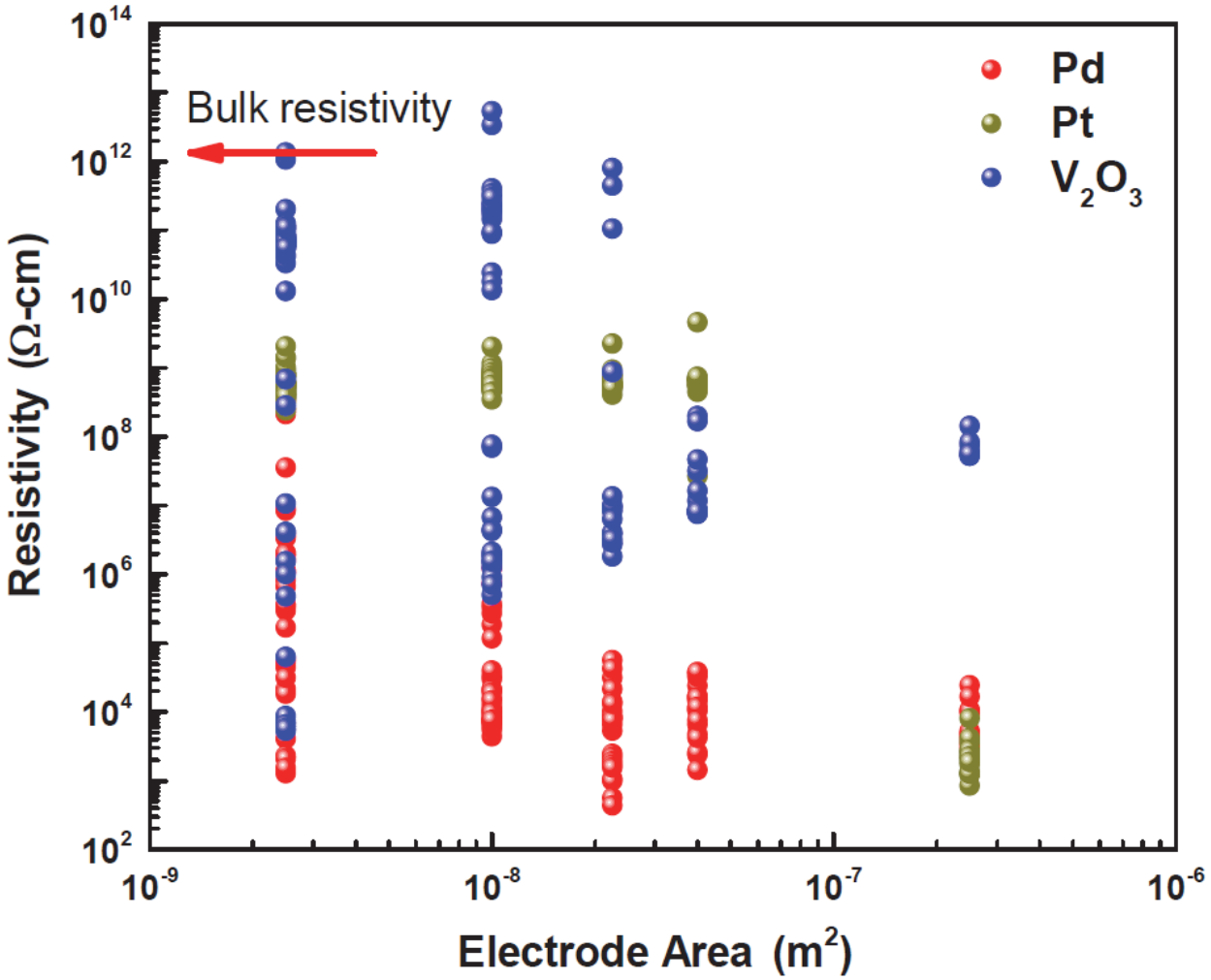

FIG. 6: Resistivity for electrodes of various sizes plotted as a function of electrode area with Pd (red data points), Pt (olive data points) and V_2O_3 (blue data points) under layers. The red arrow marks the resistivity of bulk chromia.

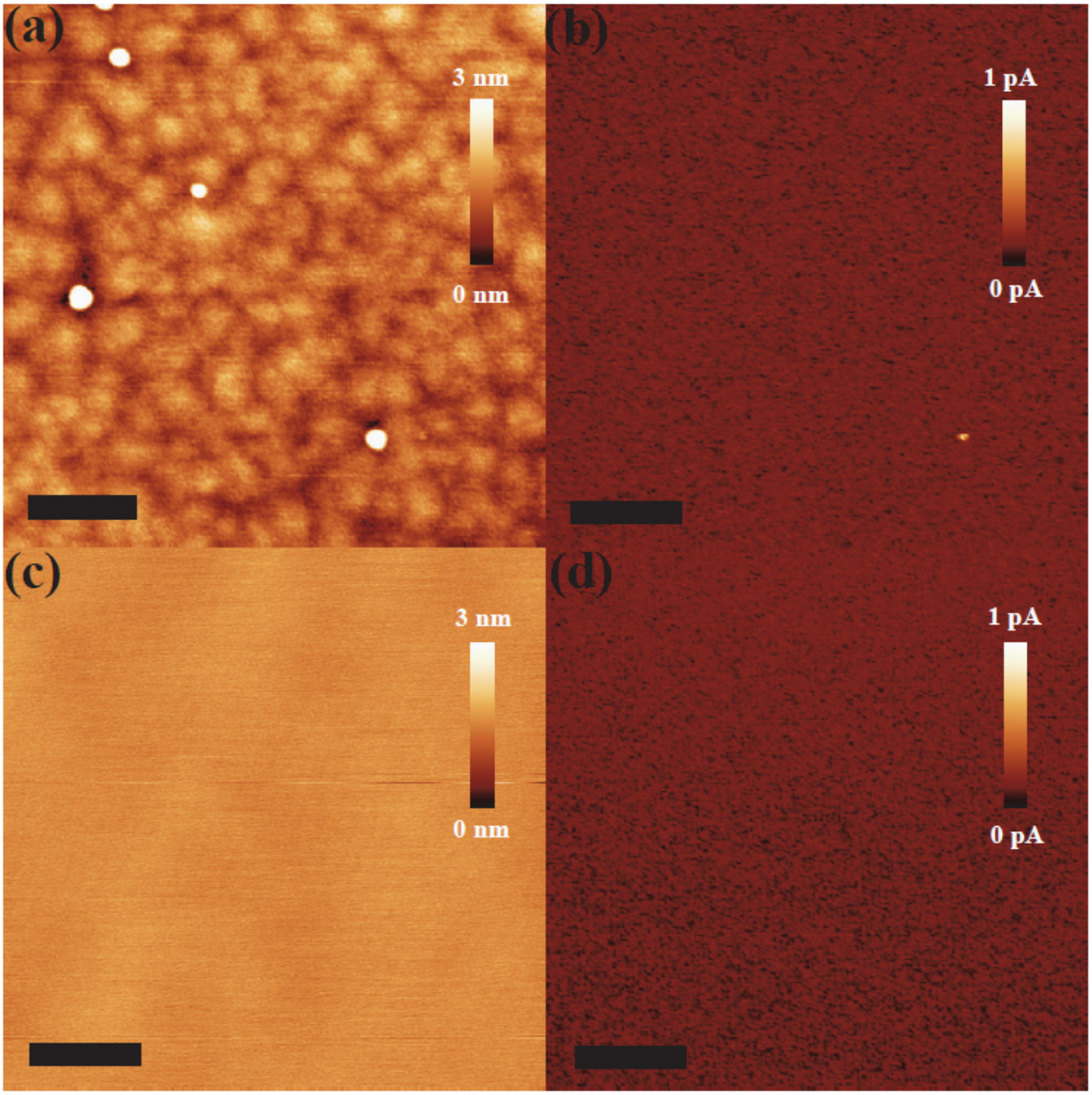

FIG. 7: Topography (a), and conduction mapping (b), of 300 nm Cr_2O_3 (0001) film on Pt seeding layer on Al_2O_3 substrate. Tip bias: 1.0 V (c) Topography of ultra-smooth surface of Cr_2O_3 (0001) on V_2O_3 (0001) seeding layer and its corresponding conductive mapping in (d). Tip bias: 3.0 V. Scale bar: 200 nm.

TABLE 1: Current measured by C-AFM tip for various electrode sizes

Pad size	**Current at V_{tip} = 1.0 V**
300 x 300 µm	1.1 nA
120 x 120 µm	0.9 nA
70 x 70 µm	0.7 nA
50 x 50 µm	0.4 nA
20 x 20 µm	0.15 nA